Chapter 27 – NUMERICAL SOLUTIONS FOR THE VFE-2 CONFIGURATION ON STRUCTURED GRIDS AT NLR, THE NETHERLANDS

by

Okko J. Boelens

27.1 INTRODUCTION

The analysis of vortex-dominated flows is of great importance for the assessment of the aerodynamics, the stability and control characteristics, the aero-elastics and the structural dynamics of fighter aircraft. The importance of vortical flow to fighter aircraft manifests itself for example as follows:

- *Aerodynamics:* Manoeuvring capabilities depend critically on vortex-induced lift; maximum vortex-induced lift is affected by vortex stability.
- *Stability and control characteristics:* The roll stability of complete fighter aircraft can heavily depend on asymmetric vortex breakdown.
- *Aero-elastics:* Unsteady vortex flow can affect the flutter speed and the level of limit cycle oscillations.
- *Structural dynamics:* Fatigue life of tail surfaces and ventral fins depends significantly on the unsteady aerodynamic energy input to the vibrations of these surfaces; this energy input can be due to vortices.

These observations motivate the investigation of the ability of CFD codes to capture the details of vortical flows around generic configurations such as delta wings.

In the late 1990s, the Netherlands National Aerospace Laboratory NLR performed an assessment of its ENFLOW flow simulation system using the data available from experiments carried out by Chu and Luckring in the National Transonic Facility (NTF) at NASA Langley ([27-1]-[27-4]). These experiments considered a 65° delta wing with four leading edge profiles (one sharp and three rounded with small, medium and large radii) for a wide range of conditions both subsonic and transonic and for both test and flight Reynolds numbers, and were used again during the second International Vortex Flow Experiment (VFE-2) ([27-5] and [27-6]), a facet of the NATO RTO AVT-113 Task Group, which was set up to consider the flow behaviour both experimentally and computationally over the 65° delta wing geometry.

Results of this investigation by NLR, more specifically results obtained for the sharp leading edge delta wing and the large radius leading edge delta wing, were presented during the bi-annual meetings of the NATO RTO AVT-113 Task Group, and are the subject of this chapter. Based on the geometry description of both delta wings ([27-1] and [27-4]), structured (multi-block) grids were generated at NLR. The grids used in simulations will be discussed in Section 27.2. Section 27.3 will discuss the important features of the flow solver ENSOLV, which is part of NLR's flow simulation system ENFLOW. Section 27.4 will discuss some of the results obtained at NLR. A section with concluding remarks (Section 27.5) completes the chapter.

27.2 GRID

At NLR the following structured (multi-block) grids have been generated using the grid generation algorithms, which are part of NLR's ENFLOW flow simulation system [27-7]:

- A baseline grid around the sharp leading edge delta wing consisting of 12 blocks, 2,048,000 grid cells and 2,169,180 grid points (see Figure 27-1 (a)).
- A baseline grid around the large radius leading edge delta wing consisting of 12 blocks, 2,048,000 grid cells and 2,169,180 grid points.
- For each flow condition considered, an adapted grid around the large radius leading edge delta wing consisting of 12 blocks, 2,048,000 grid cells and 2,169,180 grid points (see Figure 27-1 (b) for $M_\infty = 0.85$, $\alpha = 10.2°$, $Re_{mac} = 60 \times 10^6$). The baseline grid around the large radius leading edge delta wing is adapted to a computed flow solution, such that after re-computation on the adapted grid, a flow solution with higher numerical accuracy is obtained. The topological structure of the multi-block grid is maintained. The number of grid points in each block and also the geometry of the block faces are kept fixed. In each block the grid points are re-distributed based on the modified anisotropic diffusion equations developed at NLR. Corrections are used at block interfaces in order to obtain a continuous grid across block boundaries. Details can be found in [27-8]. For the large radius leading edge delta wing only results obtained on these grids are presented.

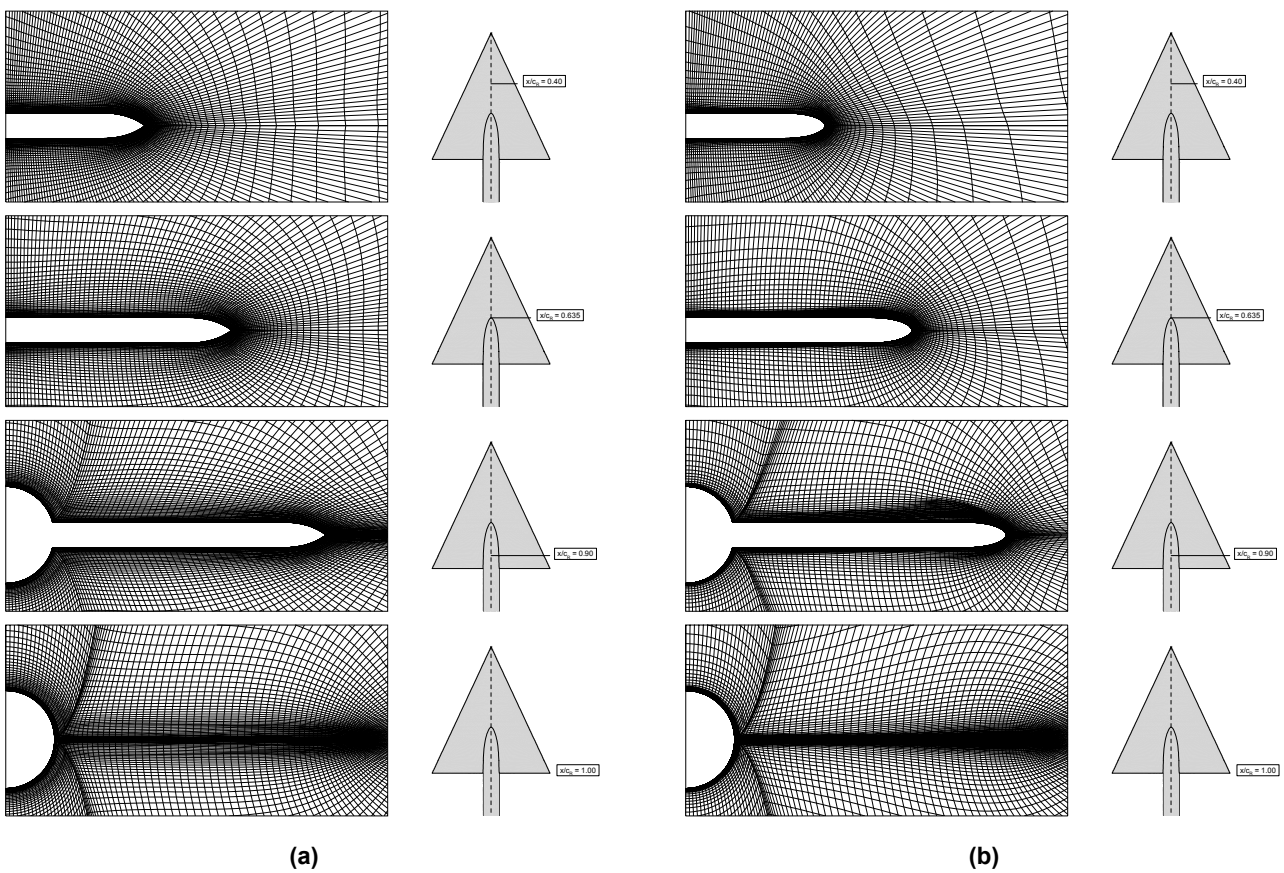

Figure 27-1: Computational Grid in Four Cross-Flow Planes: (a) Grid for the Sharp Leading Edge Wing; (b) Adapted Grid for the Large Radius Leading Edge Configuration at $M_\infty = 0.85$, $\alpha = 10.2°$, $Re_{mac} = 60 \times 10^6$.

27.3 FLOW SOLVER

The flow solver ENSOLV (version 3.23 has been used for the present study), which is part of NLR's flow simulation system ENFLOW [27-7], is capable of solving the Euler and Navier-Stokes equations on multi-block structured grids for arbitrary configurations. The configuration can be either fixed or moving relative to an inertial reference frame, and can be either rigid or flexible.

The flow equations are cast into a full conservation form employing the density ρ, the components of the momentum vector $\rho\mathbf{u}$ and the total energy per unit volume ρE as dependent variables. The equations are non-dimensionalized using the free-stream static pressure, the free-stream density, the free-stream temperature and a reference length (for example the reference wing chord).

The equations in full conservation form are discretized in space by a second-order accurate, cell-centred, finite-volume method, using multi-block structured grids, central differences, and matrix artificial diffusion. The artificial diffusion consists of a blending of second-order and fourth-order differences with a Jameson-type shock sensor for the basic flow equations and a TVD discontinuity sensor for the turbulence model equations.

For steady flow simulations, the discretized time-dependent system of equations is integrated toward the steady-state solution using a five-stage explicit Runge-Kutta scheme. Local-time stepping, implicit residual averaging and multi-grid acceleration techniques are applied.

For all computations in the present study, the original Wilcox k-ω turbulence model with cross diffusion is employed.

For more details on the flow solver ENSOLV, see also Chapter 5.

27.4 RESULTS

27.4.1 Sharp Leading Edge Delta Wing

Results obtained for the sharp leading edge delta wing are shown in Appendix 27-1. Simulations were performed for the following conditions: $M_\infty = 0.85$, $\alpha = 10.4$ or $14.5°$ and Re = 6 or 36 x 10^6.

27.4.2 Large Radius Leading Edge Delta Wing

Results obtained for the large radius leading edge delta wing are shown in Appendix 27-2. Simulations were performed for the following conditions: $M_\infty = 0.85$, $(\alpha, Re_{mac}) = (10.4°, 6 \times 10^6)$, $(10.2°, 36 \times 10^6)$, (10.2 or 14.4°, 60×10^6) or $(10.4°, 120 \times 10^6)$.

27.5 CONCLUDING REMARKS

Results of an investigation on the sharp leading edge delta wing and the large radius leading edge delta wing performed by NLR have been presented. It has been shown that agreement between computations and experiments for the sharp leading edge delta wing is good. For the large radius leading edge delta wing the agreement is much poorer. This is mainly caused by the difference in the experimental and computed location where the primary separation occurs along the round leading edge and the subsequent differences in the vortical flow structure on the upper part of the wing.

The results shown are representative for the capabilities of the flow solver during the late 1990s. Since then much progress has been made in the turbulence models used for such simulations (see [27-9] and [27-10]). Recently obtained results can be found in Chapter 5, 16 and 29.

27.6 REFERENCES

[27-1] Chu, J. and Luckring, J.M.: *Experimental Surface Pressure Data Obtained on a 65° Delta Wing Across Reynolds Number and Mach Number Ranges: Volume 1 – Sharp Leading Edge*, NASA Technical Memorandum 4645, NASA Langley Research Centre, February 1996.

[27-2] Chu, J. and Luckring, J.M.: *Experimental Surface Pressure Data Obtained on a 65° Delta Wing Across Reynolds Number and Mach Number Ranges: Volume 2 – Small Radius Leading Edge*, NASA Technical Memorandum 4645, NASA Langley Research Centre, February 1996.

[27-3] Chu, J. and Luckring, J.M.: *Experimental Surface Pressure Data Obtained on a 65° Delta Wing Across Reynolds Number and Mach Number Ranges: Volume 3 – Medium Radius Leading Edge*, NASA Technical Memorandum 4645, NASA Langley Research Centre, February 1996.

[27-4] Chu, J. and Luckring, J.M.: *Experimental Surface Pressure Data Obtained on a 65° Delta Wing Across Reynolds Number and Mach Number Ranges: Volume 4 – Large Radius Leading Edge*, NASA Technical Memorandum 4645, NASA Langley Research Centre, February 1996.

[27-5] Hummel, D. and Redeker, G.: *A New Vortex Flow Experiment for Computer Code Validation*, In Proceedings of the RTO-AVT Symposium on "Advanced Flow Management: Part A – Vortex Flows and High Angle of Attack for Military Vehicles" – RTO-MP-069(I), Pages 8.1-8.32. NATO RTO, 2001.

[27-6] Hummel, D.: *The Second International Vortex Flow Experiment (VFE-2): Objectives and First Results*, 2nd International Symposium on "Integrating CFD and Experiments in Aerodynamics", 5-6 September 2005, Cranfield University, UK. J. Aerospace Engineering, Vol. 220 (2006), No. 6: 559-568.

[27-7] *ENFLOW: A Computer Code System for Accurate Simulation of Three-Dimensional Flows*, URL: http://www.nlr.nl/documents/flyers/f222-01.pdf [cited July 2008].

[27-8] Hagmeijer, R.: *Grid Adaption Based on Modified Anisotropic Diffusion Equations Formulated in the Parametric Domain*, Journal of Computational Physics, Vol. 115, pp. 169-183, 1994.

[27-9] Kok, J.C.: *Resolving the Dependence on Free-Stream Values for the k-ω Turbulence Model*, NLR-TP-99295. 1999.

[27-10] Brandsma, F.J., Kok, J.C., Dol, H.S. and Elsenaar, A.: *Leading Edge Vortex Flow Computations and Comparison with DNW-HST Wind Tunnel Data*, NLR-TP-2001-238, 2001.

Appendix 27-1: Sharp Leading Edge Delta Wing

Figure 27-2 shows a comparison of the computed upper surface pressure distributions. In addition, the projections of the vortex core trajectory obtained by the experiment and the computations are compared. These vortex core trajectories were detected from the upper surface minimum pressure. The agreement between the computed and experimental vortex core trajectories is good.

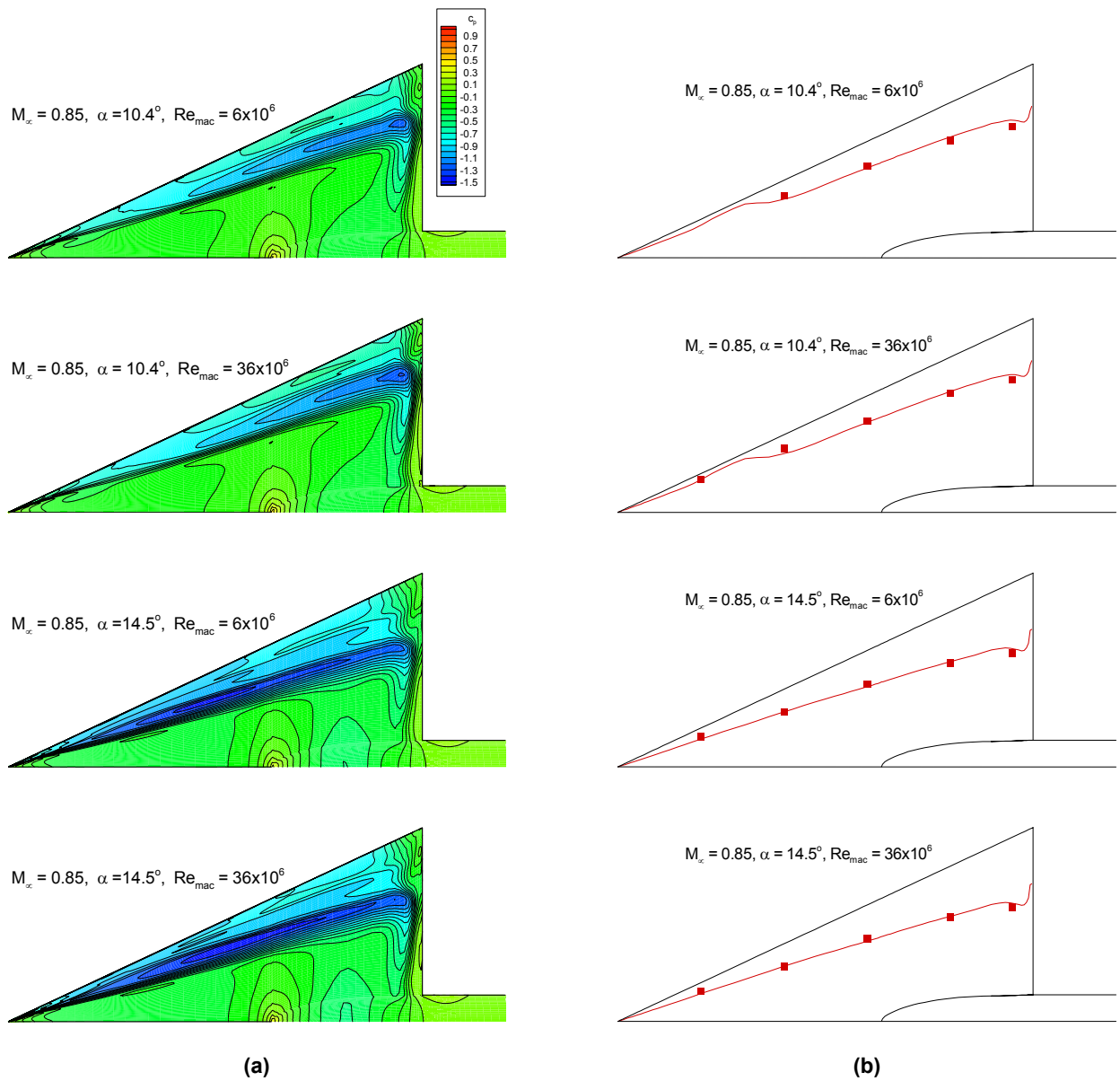

Figure 27-2: Comparison of Computed Distributions for the Sharp Leading Edge Delta Wing (M_∞ = 0.85, α = 10.4° or 14.5°, Re_{mac} = 6 or 36 x 10^6): (a) Upper Surface Pressure Distributions; (b) Projections of the Vortex Core Trajectory as Detected from Upper Surface Minimum Pressure (lines: simulation, symbols: experiment).

In Figure 27-3, a comparison of the computed and experimental upper surface peak pressure along the vortex trajectories (see also Figure 27-2) is presented. For both angles of attack the agreement is fair.

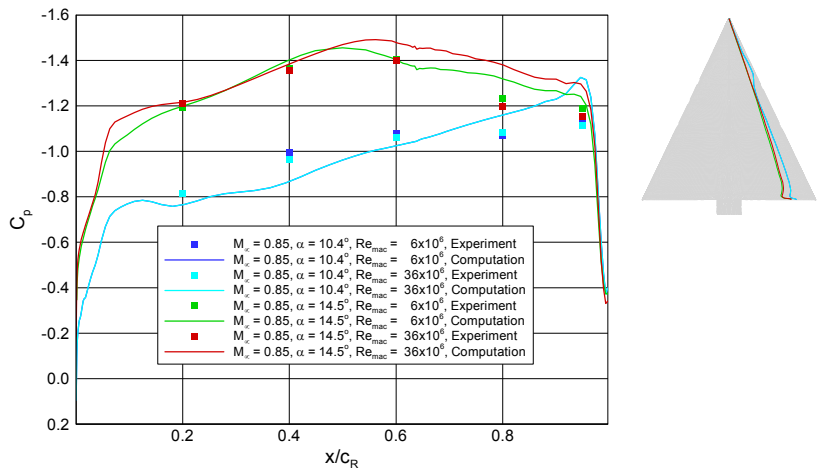

Figure 27-3: Comparison of Computed and Experimental Upper Surface Peak Pressures along Vortex Trajectory for the Sharp Leading Edge Delta Wing (M_∞ = 0.85, α = 10.4° or 14.5°, Re_{mac} = 6 or 36 x 10^6) (lines: simulation, symbols: experiment).

Figure 27-4 and Figure 27-5 show a comparison of the computed and experimental spanwise pressure distribution at x/c_r = 0.60 and x/c_r = 0.80, respectively. At both chordwise stations good agreement between the experiment and the computations is shown. The observed Reynolds number effects are small.

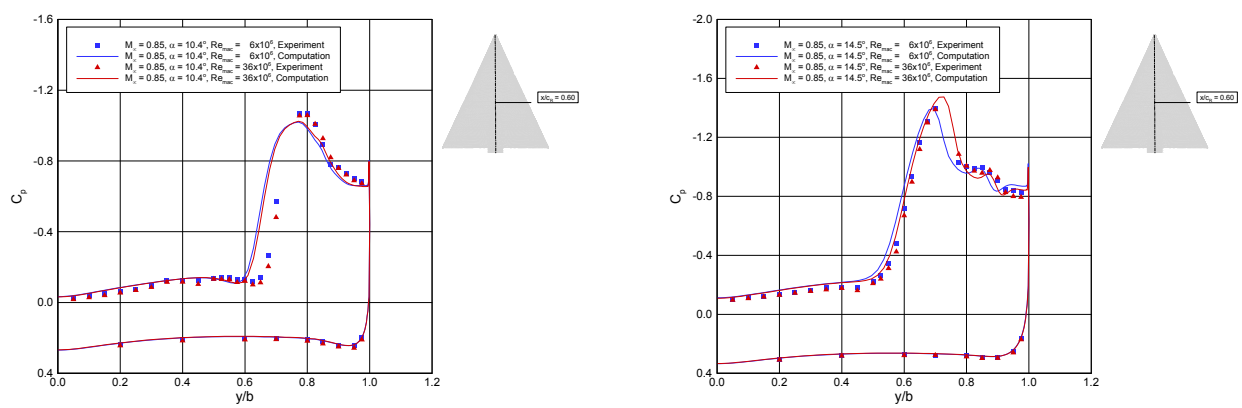

(a) **(b)**

Figure 27-4: Comparison of Computed and Experimental Spanwise Pressure Distributions for the Sharp Leading Edge Wing at x/c_r = 0.60: (a) M_∞ = 0.85, α = 10.4°, Re_{mac} = 6 or 36 x 10^6; (b) M_∞ = 0.85, α = 14.5°, Re_{mac} = 6 or 36 x 10^6.

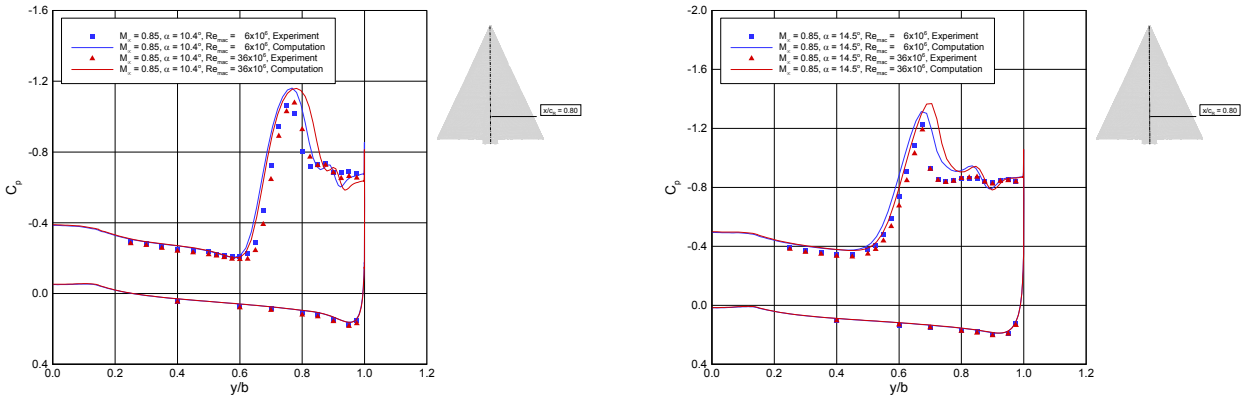

(a) **(b)**

Figure 27-5: Comparison of Computed and Experimental Spanwise Pressure Distributions for the Sharp Leading Edge Wing at x/c_r = 0.80: (a) M_∞ = 0.85, α = 10.4°, Re_{mac} = 6 or 36 x 10^6; (b) M_∞ = 0.85, α = 14.5°, Re_{mac} = 6 or 36 x 10^6.

Figure 27-6 shows the computed separation and re-attachment patterns on the upper surface for the following conditions: M_∞ = 0.85, α = 10.4° and Re = 6 x 10^6 and M_∞ = 0.85, α = 14.5° and Re = 36 x 10^6. In addition, Figure 27-7 shows the influence of the Reynolds number on the position of the upper surface separation and re-attachment lines for all simulated conditions. From these figures, it can be seen that the secondary separation starts halfway at the wing for α = 10.4°, whereas for α = 14.5° it starts right at the apex. In addition, the extent of the trailing edge separation region is increased in the spanwise direction going from α = 10.4° to α = 14.5°. Furthermore, the observed Reynolds numbers effects are small.

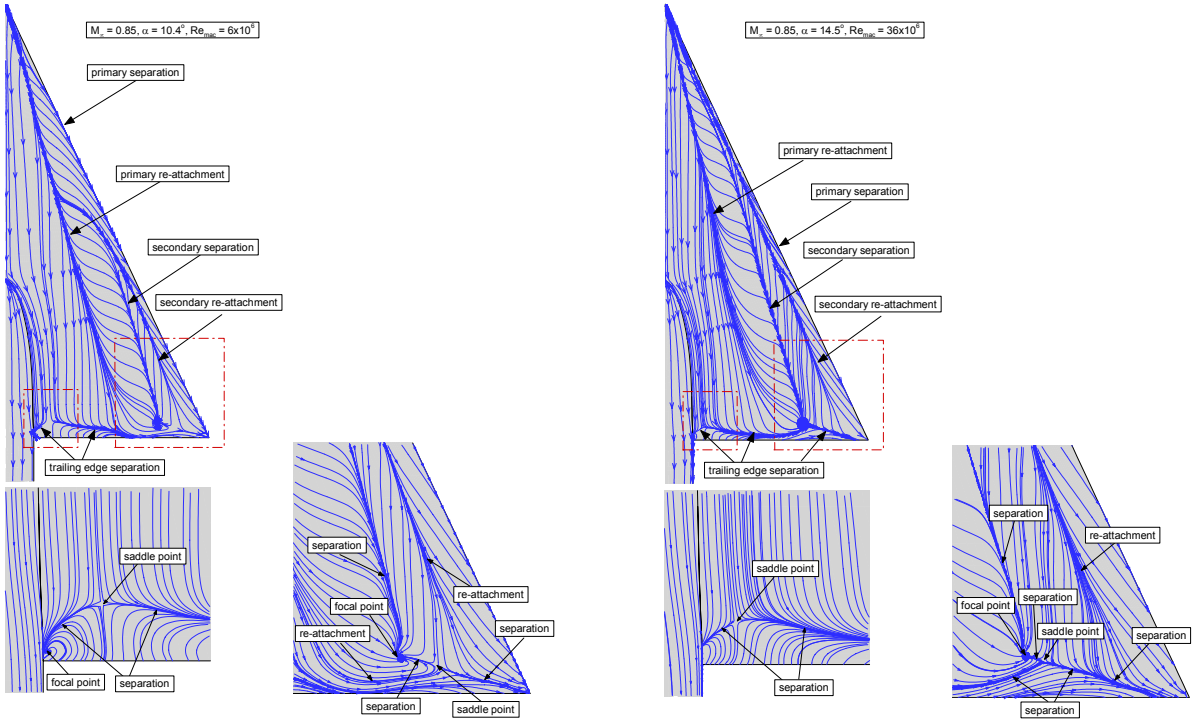

(a) (b)

Figure 27-6: Topology of Computed Separation and Re-attachment Patterns on the Upper Surface of the Sharp Leading Edge Delta Wing: (a) $M_\infty = 0.85$, $\alpha = 10.4°$, $Re_{mac} = 6 \times 10^6$; (b) $M_\infty = 0.85$, $\alpha = 14.5°$, $Re_{mac} = 36 \times 10^6$.

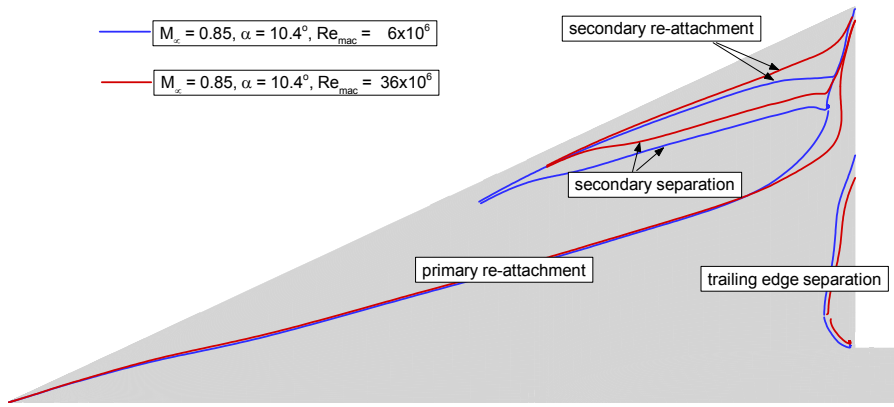

(a)

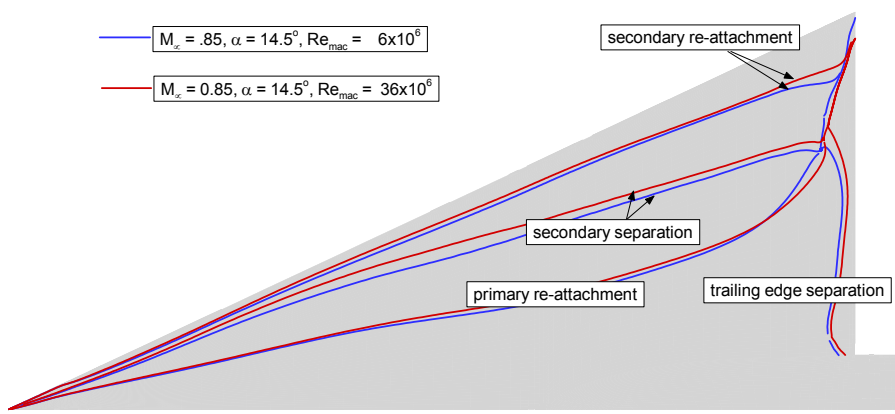

(b)

Figure 27-7: Influence of Reynolds Number on the Position of the Upper Surface Separation and Re-attachment Lines for the Sharp Leading Edge Delta Wing: (a) M_∞ = 0.85, α = 10.4°, Re_{mac} = 6 or 36 x 10^6; (b) M_∞ = 0.85, α = 14.5°, Re_{mac} = 6 or 36 x 10^6.

Finally, Figure 27-8 presents a comparison of the computed and experimental normal force and pitch moment coefficient as function of the angle of attack. The normal force coefficient shows excellent agreement. For the pitch moment coefficient, however, a constant positive shift ($\Delta C_m = C_{m\ computation} - C_{m\ experiment} \sim 0.025$) is observed.

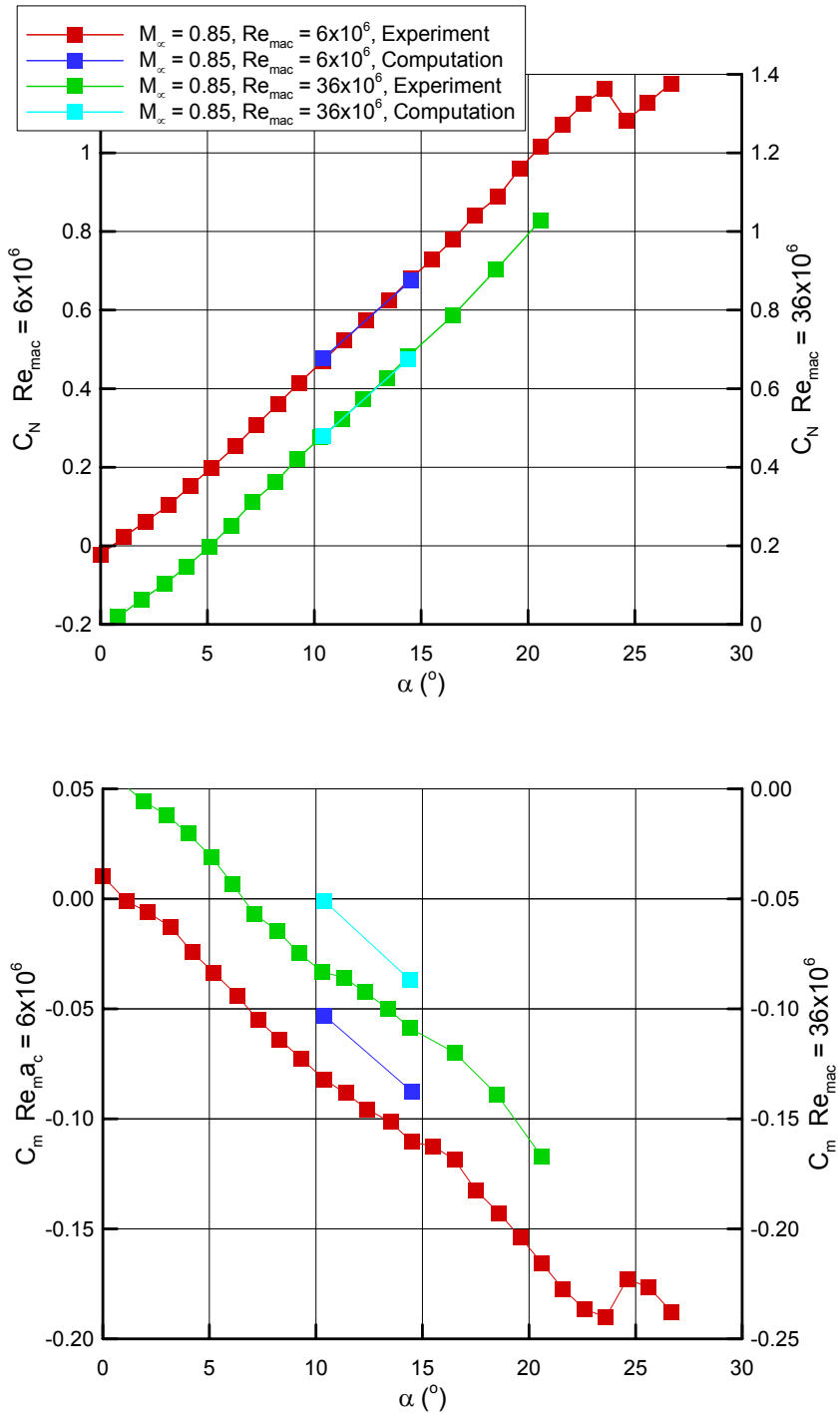

Figure 27-8: Comparison of Computed and Experimental Normal Force and Pitch Moment Coefficient as a Function of Angle of Attack for the Sharp Leading Edge Delta Wing.

Appendix 27-2: Large Radius Leading Edge Delta Wing

Figure 27-9 shows a comparison of the computed upper surface pressure distributions. In addition, the projections of the vortex core trajectory obtained by the experiment and the computations are compared. These vortex core trajectories were detected from the upper surface minimum pressure. The vortices seem to originate more aft on the delta wing in the computations than during the experiment. Whereas in the experiment already a vortex core trajectory is found at $x/c_r = 0.60$, in the simulations the vortex core trajectory can only be determined after approximately $x/c_r = 0.75$.

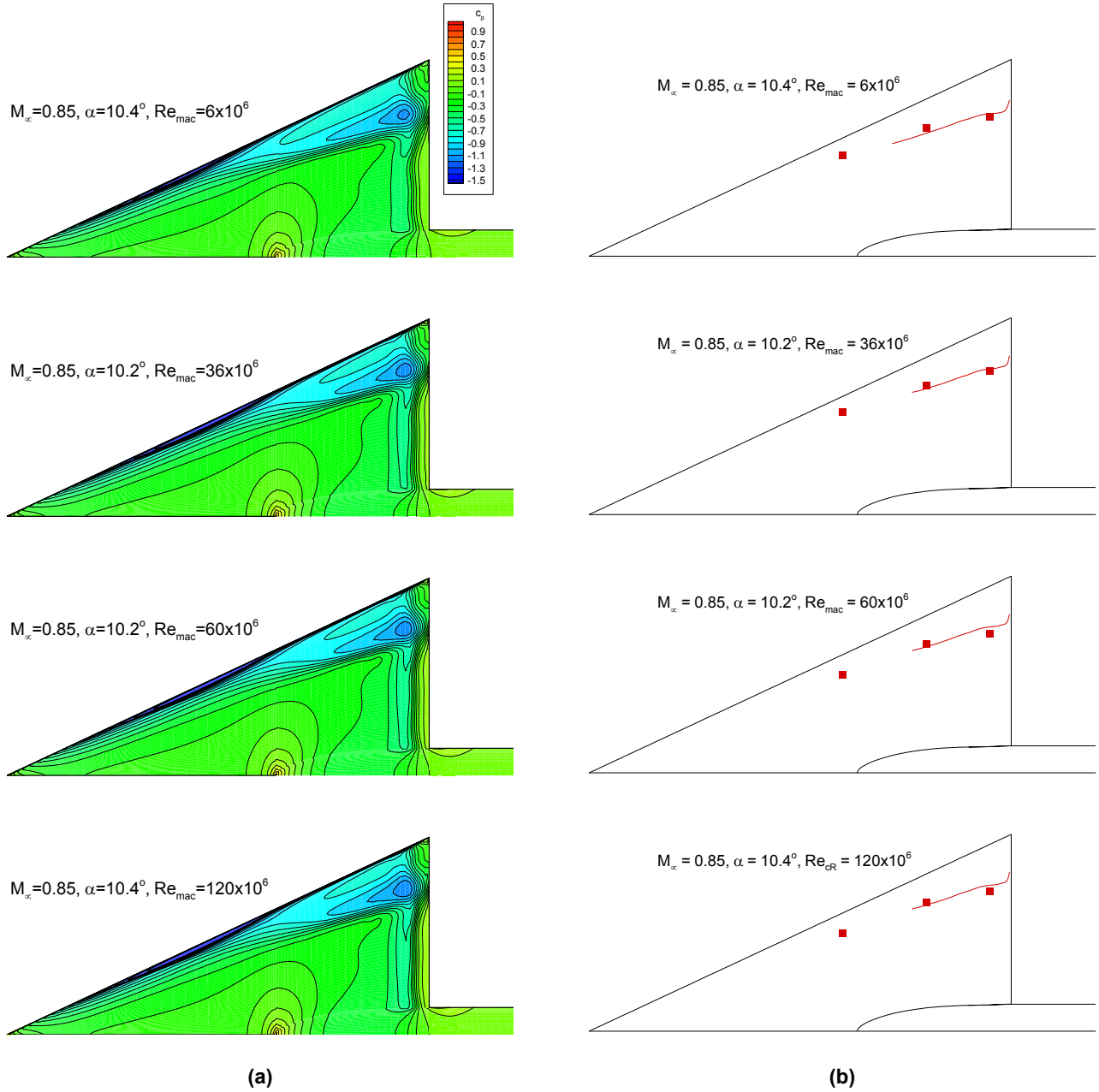

Figure 27-9: Comparison of Computed Distributions for the Large Radius Leading Edge Delta Wing (M_∞ = 0.85, (α,Re_{mac}) = (10.4°, 6 x 10^6), (10.2°, 36 x 10^6), (10.2°, 60 x 10^6) or (10.4°, 120 x 10^6)): (a) Upper Surface Pressure Distributions; (b) Projections of the Vortex Core Trajectory as Detected from Upper Surface Minimum Pressure (lines: simulation, symbols: experiment).

In Figure 27-10, a comparison of the computed and experimental upper surface peak pressure along the vortex trajectories (see also Figure 27-9) is presented. The agreement found is poor. This is mainly caused by the difference in the experimental and computed location where the primary separation occurs along the round leading edge and the subsequent differences in the vortical structure on the upper part of the wing.

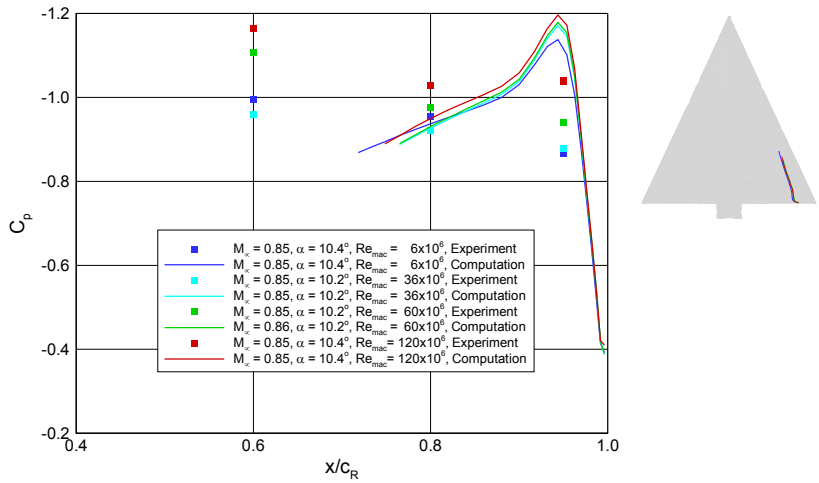

Figure 27-10: Comparison of Computed and Experimental Upper Surface Peak Pressures along Vortex Trajectory for the Large Radius Leading Edge Delta Wing (M_∞ = 0.85, (α,Re_{mac}) = (10.4°, 6 x 10^6), (10.2°, 36 x 10^6), (10.2°, 60 x 10^6) or (10.4°, 120 x 10^6)) (lines: simulation, symbols: experiment).

Figure 27-11 and Figure 27-12 show a comparison of the computed and experimental spanwise pressure distribution at x/c_r = 0.60 and x/c_r = 0.80, respectively. At x/c_r = 0.60 the agreement between the computations and the experiment is poor for all Reynolds numbers at α = 10.2 resp. 10.4°. Again, this is mainly caused by the difference in the experimental and computed location where the primary separation occurs along the round leading edge and the subsequent differences in the vortical structure on the upper part of the wing. However, at x/c_r = 0.80 the agreement is good. At α = 14.4° good agreement is obtained at x/c_r = 0.60. However, at x/c_r = 0.80 the pressure peak is over predicted in the simulations.

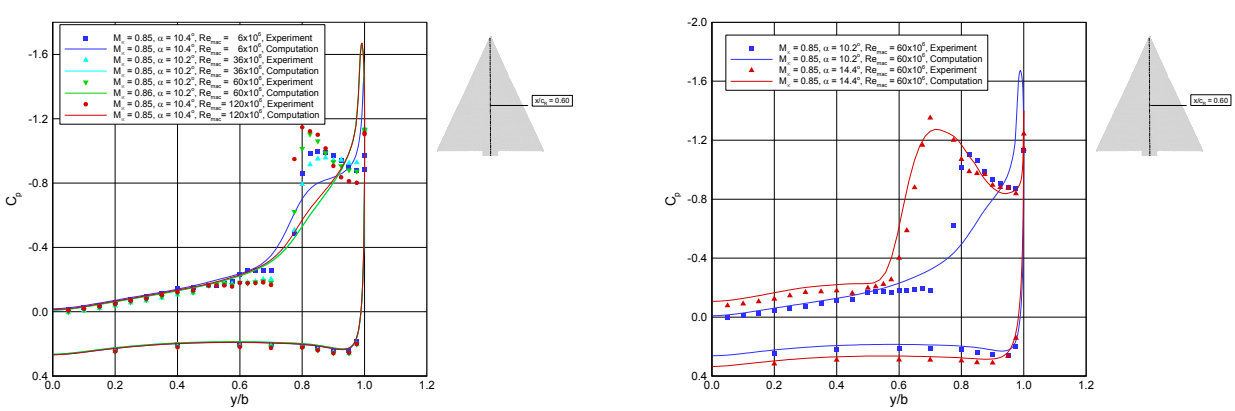

(a) **(b)**

Figure 27-11: Comparison of Computed and Experimental Spanwise Pressure Distributions for the Large Radius Leading Edge Wing at x/c_r = 0.60: (a) M_∞ = 0.85, (α,Re_{mac}) = (10.4°, 6 x 10^6), (10.2°, 36 x 10^6), (10.2°, 60 x 10^6) or (10.4°, 120 x 10^6); (b) M_∞ = 0.85, α = 10.2 or 14.4°, Re_{mac} = 60 x 10^6.

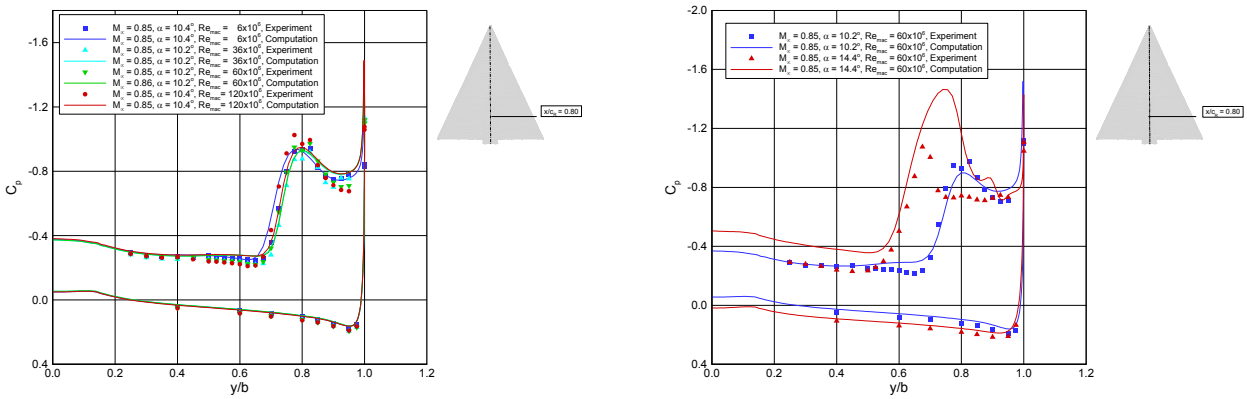

(a) **(b)**

Figure 27-12: Comparison of Computed and Experimental Spanwise Pressure Distributions for the Large Radius Leading Edge Wing at x/c_r = 0.80: (a) M_∞ = 0.85, (α,Re_{mac}) = (10.4°, 6 x 10^6), (10.2°, 36 x 10^6), (10.2°, 60 x 10^6) or (10.4°, 120 x 10^6); (b) M_∞ = 0.85, α = 10.2° or 14.4°, Re_{mac} = 60 x 10^6.

Figure 27-13 shows the computed separation and re-attachment patterns on the upper surface for the following conditions: M_∞ = 0.85, α = 10.4° and Re = 6 x 10^6. To see the effect of the leading edge geometry on the flow topology, this figure should be compared with Figure 27-6 (a). Figure 27-14 shows the influence of the Reynolds number on the position of the upper surface separation and re-attachment lines for all simulated conditions at α = 10.2° resp. 10.4°. Going from Re_{mac} = 6 x 10^6 to 36 x 10^6 both the primary re-attachment line and the trailing edge separation move aft on the wing upper surface. For Reynolds numbers larger than 36 x 10^6 the observed Reynolds numbers effects are, however, small.

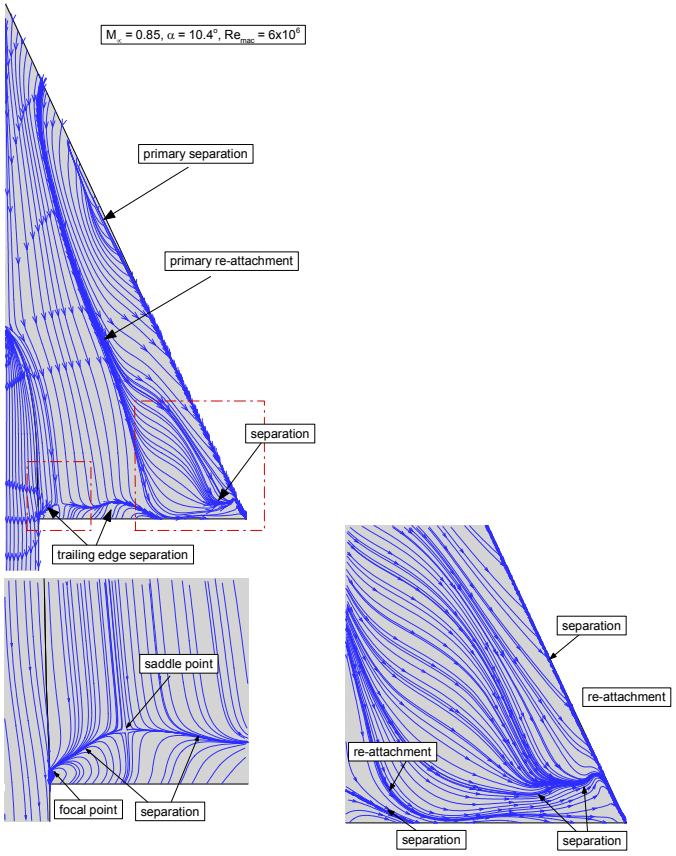

Figure 27-13: Topology of Computed Separation and Re-attachment Patterns on the Upper Surface of the Large Radius Leading Edge Delta Wing (M_∞ = 0.85, α = 10.4°, Re_{mac} = 6 x 10^6).

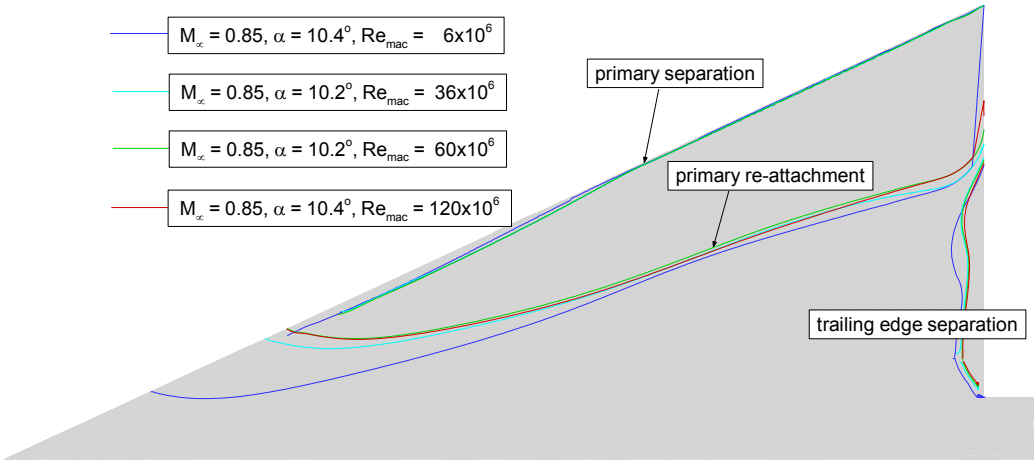

Figure 27-14: Influence of Reynolds Number on the Position of the Upper Surface Separation and Re-attachment Lines for the Large Radius Leading Edge Delta Wing (M_∞ = 0.85, (α,Re_{mac}) = (10.4°, 6 x 10^6), (10.2°, 36 x 10^6), (10.2°, 60 x 10^6) or (10.4°, 120 x 10^6)).